A surface flattening method for characterizing the surface stress, drained Poisson's ratio and diffusivity of poroelastic gels

Zezhou Liu¹, Chung-Yuen Hui^{1,2*}, Anand Jagota³, Jian Ping Gong^{2,4,5}, and Ryuji Kiyama⁶

¹Field of Theoretical and Applied Mechanics, Sibley School of Mechanical and Aerospace Engineering, Cornell

University, Ithaca, NY 14853, USA

²Global Station for Soft Matter, GI-CoRE, Hokkaido University, Sapporo, Japan

³Departments of Bioengineering and of Chemical & Biomolecular Engineering, 111 Research Drive, Lehigh

University, Bethlehem, PA 18015, USA

⁴Faculty of Advanced Life Science, Hokkaido University, Sapporo 001-0021, Japan

⁵WPI-ICReDD, Hokkaido University, Sapporo 001-0021, Japan

⁶Graduate School of Life Science, Hokkaido University, Sapporo 001-0021, Japan

*Corresponding Author: Chung-Yuen Hui (ch45@cornell.edu)

Abstract: When a poroelastic gel is released from a patterned mold, surface stress drives deformation and solvent migration in the gel and flattens its surface profile in a time-dependent manner. Specifically, the gel behaves like an incompressible solid immediately after removal from the mold, and becomes compressible as the solvent is able to squeeze out of the polymer network. In this work, we use the finite element method (FEM) to simulate this transient surface flattening process. We assume that the surface stress is isotropic and constant, the polymer network is linearly elastic and isotropic, and that solvent flow obeys Darcy's law. The short-time and long-time surface profiles can be used to determine the surface stress and drained Poisson's ratio of the gel. Our analysis shows that the drained Poisson's ratio and the diffusivity of the gel can be obtained using interferometry and highspeed video microscopy, without mechanical measurement.

Keywords: surface flattening, surface stress, poroelasticity, Darcy's law, diffusivity, drained Poisson's ratio

1. Introduction

Most conventional engineering materials resist deformation by their bulk mechanical properties, such as elasticity, plasticity, and the like. For these materials, the mechanical role of the surface is utterly negligible.

1

However, when a material is soft enough, surface stress is known to play a significant and sometimes dominant role, requiring re-thinking a wide range of mechanical phenomena and properties 1,2 . Surface stress effects are typically felt over a characteristic length scale, the elasto-capillary length, $l_c \sim \sigma_s / E$, where E is Young's modulus of the bulk and σ_s is the magnitude of the surface stress. For conventional stiff materials (e.g., metals and ceramics), the value of elasto-capillary length is immeasurably small, on the order of angstroms. For soft solids, such as elastomers and gels with elastic modulus in the MPa to kPa range, respectively, the corresponding value of elasto-capillary length is on the order of tens of nanometers to tens of microns or larger. This affects a wide range of interesting phenomena and properties. For instance, surface stress can flatten sharp features by smoothing corners and undulations $^{3-5}$, drive instabilities 6 , stiffen fluid-solid composites 7 , significantly affect the opening of cracks $^{8-10}$, invalidate the classical theories of Hertz and Johnson-Kendall-Roberts (JKR) for contact mechanics without and with adhesion $^{11-16}$, alter solvent flow in porous media 17,18 , and invalidate the classical Young equation for partial wetting $^{1,19-28}$.

These recent investigations have addressed only the simplest constitutive behavior that a soft solid surface can have: the surface behavior is represented by an isotropic, homogeneous, and strain-independent stress, equivalent to the surface tension of simple fluid interfaces. This simple surface behavior is assumed in this work. It is a reasonable assumption since many soft solids – such as gels, elastomers, and most biomaterials – either contain a significant solvent component or have molecular structures that comprise chain-like molecules that locally are fluid-like. However, it must be noted that complex surface properties such as surface elasticity (straindependent resistance to stretching) and surface bending (resistance to surface curvature change) are known to exist in many physical systems. For example, recent experiments by Jensen et al.²⁹ have shown that soft gel surfaces can have considerable elasticity. Similar to lipid bilayers, surfaces of soft solids can also resist surface bending moments, e.g., a thin silica film that forms on the surface of an elastomer (e.g., polydimethylsiloxane) exposed to ultraviolet ozonolysis (UVO) or oxygen plasma. ^{30,31} Lapinski et al. ³² recently demonstrated that, after UVO treatment, the surface of a commonly used PDMS has significant surface stress, considerable extensional elasticity and surface bending stiffness, and their results were confirmed by a finite element analysis (FEA). Here we note that constitutive theories in which a surface can elastically resist an arbitrary amount of bending, stretching and shearing have been proposed by Steigmann and Ogden,³³ Gao et al.³⁴, Gurtin and Murdoch³⁵ and Green.³⁶. A summary of these models and some exact solutions illustrating the different manners in which surface stiffening and surface bending affect structural behavior can be found in Liu et al.³⁷

Much of the work on the role of surface stresses in soft materials has focused on time-independent elastic deformations, with few studies that handle time-dependent deformation mechanisms such as flow of solvent or viscoelasticity in the bulk ^{38–44}. Here we note that poroelasticity in soft materials has been studied for a long time

and is an active research field ^{45–49}. However, the interplay between poroelasticity and surface elasticity has begun to be considered only recently ^{17,50,51}.

There are several ways to measure poroelastic properties of gels, such as by confined compression ^{52,53}, indentation ^{48,49}, beam-bending ⁵⁴, fluorescence recovery after photobleaching (FRAP) ⁵⁵, electronic speckle pattern interferometry (ESPI) ⁵⁶, and nuclear magnetic resonance (NMR) spectroscopy ⁵⁷. For example, Hu et al. ⁴⁸ use the indentation method to determine the shear modulus, Poisson's ratio and diffusivity of hydrogels. In their test, a rigid indenter is pressed into the gel to a fixed depth, and the resulting force is recorded. The measured instantaneous force determines the shear modulus, the ratio of instantaneous and equilibrated forces determines the drained Poisson's ratio, and the force relaxation curve determines the diffusivity. However, none of these methods considers the effect of surface stress on the measurements.

The present work is partially motivated by our recent interest in developing a technique to measure surface rheology in soft solids 5,32 . This technique is shown schematically in Fig. 1(a-c). Gel samples are created by replica-molding a soft gelatin-based organogel with 70/30 glycerol/water as solvent into a much stiffer patterned PDMS master consisting of periodic ridges, as shown in Fig. 1(a). (In a previous work 58 the master mold had a rippled surface and the solvent for gelatin was water.) The initial surface height of the pattern is denoted by h_0 , and the width of the ridge and the spacing between the ridges are both equal to w. (In the previous experiments 5,32 , h_0 is about a few microns and w is on the order of tens of microns.) The length of the ridges in the out of plane direction is much larger than any relevant scales such as w and h_0 . When the gel is released from the geometric constraint at time t = 0 (the undeformed configuration just before the removal is shown in Fig. 1(b)), the surface stress of the gel-air interface flattens the gel surface instantaneously, reducing the surface height to h (Fig. 1(c)). The reduction in the heights, i.e. the peak-to-valley distances (h) of the surface features when the gel surface is exposed to air, can be measured using optical interferometry 5,32 . For the samples with a glycerol/water solvent there was insignificant subsequent deformation. Presumably, the viscosity of glycerol/water mixture was high so solvent flow was insignificant in the time frame of experiment and could be neglected.

Here we ask the following question: can we analyze quantitatively the case in which the gel has a sufficiently high permeability so solvent flow can occur? Intuitively, we expect that at the instant the gel is removed from the mold, it behaves like an incompressible elastic solid since solvent flow takes finite time. At sufficiently long times (to be specified below) the gel behaves as a compressible elastic solid (with the drained Poisson ratio ν) as solvent squeezes out of the polymer network. Hence the surface profile is expected to change over time.

Part of our goal in this work is to investigate if the time-dependent surface profile measured in experiments can be used to determine properties such as the surface stress, drained Poisson's ratio, and diffusivity of the gel without making contact with the material. In most experiments, the ridges are quite shallow (i.e., $h_0 \ll w$). As

a result, the deformation due to surface stress is sufficiently small to allow the bulk behavior to be represented by linear poroelasticity. In this work, we further assume that the chemical potential of the solvent in the gel is in equilibrium with the external solvent in the air (i.e., air with saturated humidity), hence the gel does not dry or swell.

The outline of the paper is as follows. In Section 2, we briefly review the field equations of linear poroelasticity. In Section 3, we use the finite element method (FEM) to simulate the time-dependent surface flattening process. In section 4, we then discuss how to extract material properties from the results. Summary and discussion are presented in section 5.

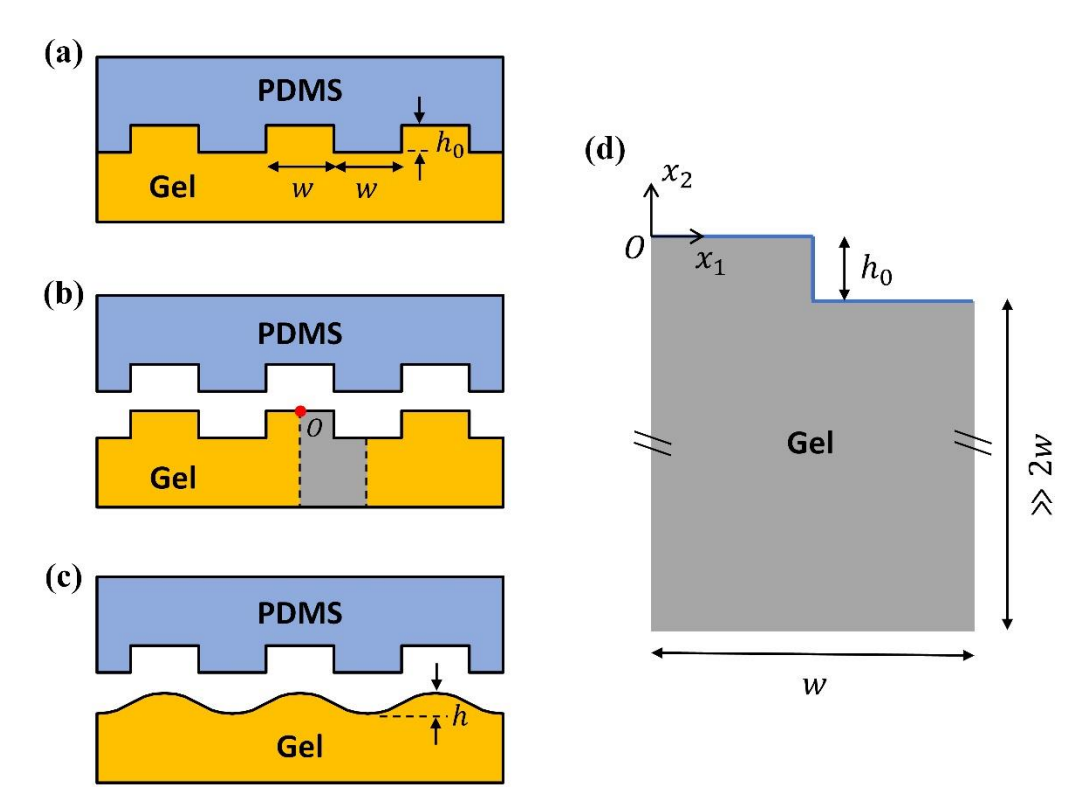


Fig. 1. (a) The soft gel is cured in a PDMS mold with periodic ridges and channels. These ridges and channels are parallel to each other and their length in the out-of-plane direction x_3 is much longer than any in-plane dimensions. (b) The shape of the gel and PDMS after release in the *absence* of surface stress. (c) The actual shape after release. Surface stress flattens the surface of the soft gel sample. Since the elastocapillary length of PDMS mold is on the order of nm, there is no observable deformation of the mold due to its surface stress. (d) Schematic of finite element model.

2. Field Equations Summary

The channels and ridges are assumed to be infinitely long in the x_3 direction. This simplification allows us to model the deformation as plane strain where the out-of-plane displacement is identically zero and the continuum

fields are independent of x_3 . For the sake of clarity, we briefly review the plane strain theory of linear poroelasticity. Details can be found in the previous works $^{59-62}$. The gel is modeled as a fully saturated, elastic, porous medium occupying a two-dimensional region Ω_0 with a surface $\partial\Omega_0$. We assume that the drained network is elastic and isotropic, while the skeleton of the network and solvent phase are incompressible. The material point position in the gel is denoted by x_{α} ($\alpha=1,2$) at time t. The time-dependent displacement filed is denoted by u_{α} . In plane strain, the out of plane strain components are identically zero, and the in-plane strain $\left(\varepsilon_{\alpha\beta}\right)$ - displacement relation is

$$\varepsilon_{\alpha\beta} = \left(u_{\alpha,\beta} + u_{\beta,\alpha}\right)/2 \text{ in } \Omega_0, \tag{1}$$

where lower-case Greek subscripts range from 1 to 2, and $()_{,\alpha}$ denotes partial derivative with respect to x_{α} , i.e., $()_{,\alpha} \equiv \partial()/\partial x_{\alpha}$. The stress-strain relation for stress tensor $\sigma_{\alpha\beta}$, strain tensor $\varepsilon_{\alpha\beta}$, and pore pressure p is

$$\sigma_{\alpha\beta} = 2G\varepsilon_{\alpha\beta} + \left(K - \frac{2G}{3}\right)\varepsilon_{\gamma\gamma}\delta_{\alpha\beta} - p\delta_{\alpha\beta} \text{ in } \Omega_0,$$
(2)

where G and K are the shear and bulk moduli of the drained network, respectively, and $\delta_{\alpha\beta}$ is the Kronecker delta. Here, summation convention over repeated indices is used. The sign convention is that stresses are positive when they are tensile, and pore pressure is positive when it is compressive. The bulk modulus K is related to the shear modulus G by

$$K = \frac{2(1+\nu)G}{3(1-2\nu)},\tag{3}$$

where v is the drained Poisson's ratio of the gel. In the absence of body forces and ignoring inertia, the stress tensor $\sigma_{\alpha\beta}$ satisfies the equilibrium equations

$$\sigma_{\alpha\beta,\beta} = 0 \text{ in } \Omega_0.$$
 (4)

Solvent flow in the gel is assumed to be governed by Darcy's law, i.e., the solvent flux J_{α} is proportional to the spatial gradient of the pore pressure p by

$$J_{\alpha} = -\frac{k}{\eta} p_{,\alpha} \,, \tag{5a}$$

where k is the permeability and η is the viscosity of the solvent. In the literature, Darcy's law often takes another form as

$$J_{\alpha} = -\frac{k_{w}}{\gamma_{w}} p_{,\alpha}, \tag{5b}$$

where k_w is the hydraulic conductivity and γ_w is the weight density of the solvent, thus $k/\eta = k_w/\gamma_w$. Combining the mass conservation, Darcy's law, and equilibrium equations, Biot ⁶⁰ showed that

$$D_c \nabla^2 \varepsilon_{\gamma \gamma} = \frac{\partial \varepsilon_{\gamma \gamma}}{\partial t}, \ D_c = \frac{2G(1-\nu)}{1-2\nu} \frac{k_w}{\gamma_{yy}}$$
 (6)

where ∇ is the 2D Laplacian. D_c is often referred to as the cooperative diffusivity of the gel.

In contrast to standard poroelasticity theory, here the gel surface supports surface stress and does work by stretching. We assume stretching of surface is resisted by a constant isotropic surface stress σ_s . The surface equilibrium equations require the discontinuity of the stress across the interface to be balanced by the Laplace pressure induced by surface stress 2,37 . For example, if the surface is traction free on $\partial\Omega_T$, we have

$$\sigma_{\alpha\beta}n_{\beta} = \sigma_{s}\kappa \text{ in } \partial\Omega_{\tau}, \tag{7}$$

where n_{β} is the unit outward normal to $\partial\Omega_{T}$, and κ is the in-plane curvature of the *deformed* surface profile. It should be noted that κ is part of the solution, making poroelastic problems more difficult to solve analytically.

3. Finite Element Analysis

Given the complexity of the field equations, it is difficult to obtain closed-form solutions. Therefore, we simulate the transient process using a finite element method (FEM). The finite element model is illustrated in Fig. 1(d) and implemented in a commercial software, ABAQUS. Due to symmetry, only a half-wavelength sample is modeled (shaded region Ω_0 in Fig. 1(b)). The initial surface height h_0 is much less than the period $\lambda = 2w$, i.e., $h_0 \ll 2w$. The thickness of the gel sample is a few times the wavelength. The polymer network is modeled as an elastic solid with a shear modulus G and drained Poisson's ratio ν . The hydraulic conductivity and weight density of the gel are k_w and γ_w , respectively, and they are assumed to be constant. The fixed coordinate system (x_1, x_2) is shown in Fig. 1(d): in the undeformed configuration, the origin O coincides with the middle point of the top flat region of the ridge-channel structure (O is labeled by the red point in Fig. 1(b)). After deformation, the material point occupies (y_1, y_2) with respect to the same coordinate system, thus $y_{\alpha} = x_{\alpha} + u_{\alpha}$. We parametrize the *deformed* surface profile by y_1 as $(y_1, y_2 = s(y_1))$. The boundary conditions are: no horizontal displacement, shear traction, or solvent flux is allowed on the left and right edges of Ω_0 ; on the bottom edge of Ω_0 , the vertical displacement, shear traction and solvent flux are all zero; and on the top edges (indicated by the blue lines in Fig. 1(d)), the pore pressure is zero and surface stress is applied. The initial condition is that pore pressure is zero everywhere in the gel. In small strain poroelastic theory, this condition states the chemical potential of solvent is continuous across the interface ⁴⁶. This condition can be satisfied by exposing the sample

to an environment of saturated solvent vapor pressure. This also prevents drying of the gel, which can drastically change its mechanical properties ^{63–66}.

Continuum coupled displacement and pore pressure elements CPE4P are used in our FEM. Special user-defined surface finite elements are attached to the top edges to model the constant surface stress. These user-defined surface elements have been reported in our previous works ²⁸.

4. Results

The following normalization is used to expedite the analysis. The normalized coordinates are $\overline{x}_1 \equiv x_1 / w$, $\overline{x}_2 \equiv x_2 / h_0$, $\overline{y}_1 \equiv y_1 / w$, and $\overline{y}_2 \equiv y_2 / h_0$. Thus, the normalized deformed surface profile is $\overline{s}\left(\overline{y}_1\right) \equiv s\left(y_1\right) / h_0$, normalized surface height is $\overline{h} \equiv h / h_0$, and the elastocapillary number is $\overline{l}_c \equiv \sigma_s / Gw$. Time t is normalized by a characteristic time t^* , which is proportional to the square of a characteristic length of the gel. There are three length scales in our problem: the initial surface height h_0 , the elasto-capillary length $h_0 = \sigma_s / G$, and the wavelength $h_0 = h$ and h_0

4.1 Surface profiles and heights at short and long times

We first consider the limiting cases of surface profiles at short and long times. The finite element results of surface profiles at $\overline{t} = 0^+$ (blue dashed line) and $\overline{t} = \infty$ (red dotted line) are plotted in Fig. 2(a), where $h_0 / w = 0.04$, $\overline{l_c} = \sigma_s / Gw = 0.2$, and v = 0.2. The surface profiles have been shifted vertically so that the lowest position in both is set to zero. Fig. 2(a) shows that the gel corners are noticeably rounded compared to its sharp-edged ridge-channel mold. The gel surface is also significantly flattened by surface stress with no change in wavelength. The gel further flattens as the solvent is squeezed out and the gel becomes more compressible, eventually reaching its equilibrium shape as $\overline{t} >> 1$.

Alternatively, the short- and long-time solutions can be obtained by studying the deformation driven by surface stress for an *elastic* solid: the instantaneous response of the porous medium behaves like an incompressible elastic solid, while at long times the porous medium behaves as a compressible elastic solid with the drained Poisson's ratio ν . Hui et al. ⁶⁷ have recently provide an analytical solution to determine the flattened surface profile for any initial surface profile of a linear elastic half space, provided that surface stress is isotropic and constant. Using our notation, the deformed surface profile is given by

$$\overline{s}\left(\overline{y}_{1}\right) = \frac{1}{2} + \sum_{n=1}^{\infty} a_{n} \cos\left(n\pi \overline{y}_{1}\right), \ a_{n} = \frac{2\sin\left(n\pi/2\right)}{n\pi \left[1 + n\pi\left(1 - v^{e}\right)\sigma_{s}/Gw\right]},\tag{8}$$

where v^e is the Poisson's ratio of the *elastic* solid. We determine the short and long times solutions using $v^e = 0.5$ and $(v^e = v = 0.2)$ in (8). These analytical results are shown as squares and circles, respectively, in Fig. 2(a). Clearly, there is a very good agreement between numerical and analytical short and long times solutions.

Next, we investigate the change in surface height during solvent flow. Let us denote the surface heights at short and long times by h_s and h_l , respectively. The corresponding normalized heights are $\overline{h}_s = h_s / h_0$ and $\overline{h}_l = h_l / h_0$ respectively. In Fig. 2(b), we plot the normalized short- and long-time surface heights versus the elasto-capillary number \overline{l}_c . As expected, our FEM shows that the surface height decreases as the elasto-capillary number increases and is further reduced as the gel relaxes over time. The surface heights \overline{h}_s and \overline{h}_l can also be computed using (8), $\overline{h}_s = \overline{s} \left(\overline{y}_1 = 0, v^e = 0.5 \right) - \overline{s} \left(\overline{y}_1 = 1, v^e = 0.5 \right)$ and $\overline{h}_l = \overline{s} \left(\overline{y}_1 = 0, v^e = 0.2 \right) - \overline{s} \left(\overline{y}_1 = 1, v^e = 0.2 \right)$, respectively. We find

$$\overline{h}_{s} = \sum_{n=1,3,\dots}^{\infty} \frac{4\sin\left(n\pi/2\right)}{n\pi\left[1 + n\pi\sigma^{s}/2Gw\right]} = \sum_{n=1,3,\dots}^{\infty} \frac{4\sin\left(n\pi/2\right)}{n\pi\left[1 + n\pi\overline{l}_{c}/2\right]},\tag{9a}$$

$$\overline{h}_{l} = \sum_{n=1,3,\dots}^{\infty} \frac{4\sin\left(n\pi/2\right)}{n\pi\left[1 + n\pi\left(1 - \nu\right)\sigma^{s}/Gw\right]} = \sum_{n=1,3,\dots}^{\infty} \frac{4\sin\left(n\pi/2\right)}{n\pi\left[1 + n\pi\left(1 - \nu\right)\overline{l}_{c}\right]}.$$
(9b)

The analytical predictions are plotted as symbols in Fig. 2(b) for comparison. Again, they match well at the two limits of short and long times.

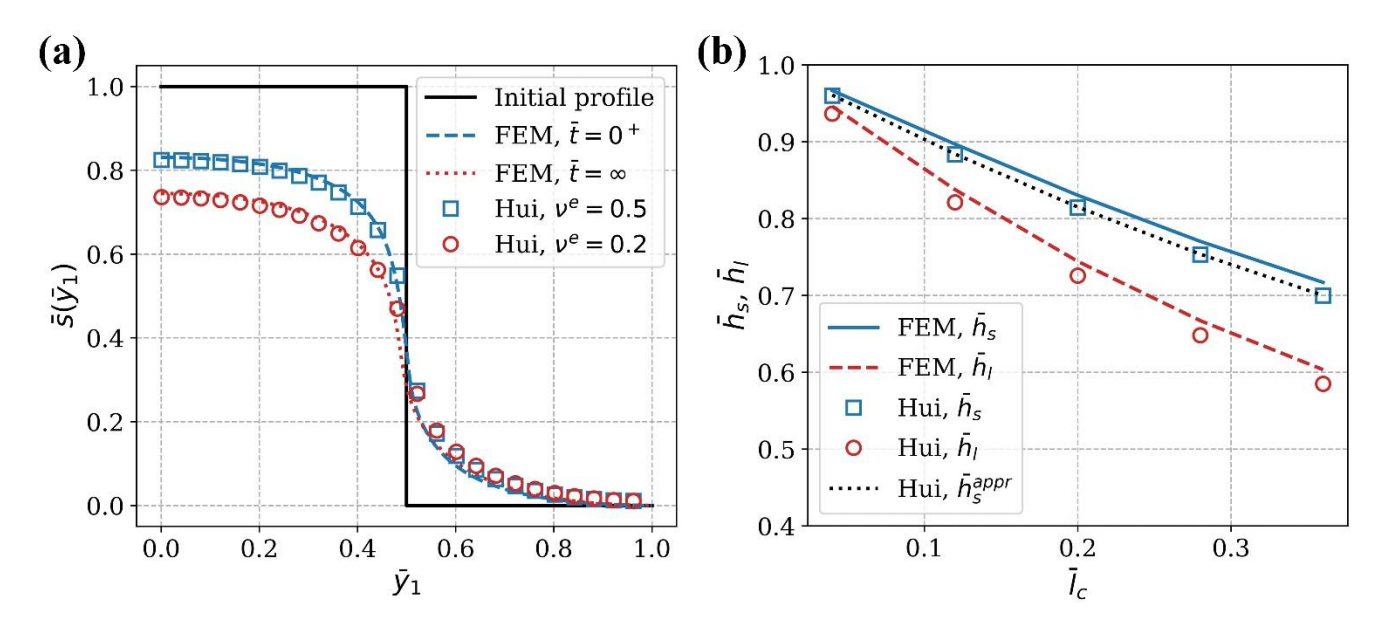


Fig. 2. (a) Initial profile of the gel surface (black solid line), comparison of FEM solution (blue dotted line) with analytical solution (8) (for $v^e = 0.5$, squares) just after gel is release from mold $(t = 0^+)$; comparison of FEM profile at long times (red dotted line) with (8) (for $v^e = v = 0.2$, circles). (b) Normalized surface height for short (blue) and long times (red) versus elasto-capillary number $\overline{l_c}$. Analytical results are represented by squares and circles, and FEM results are represented by dotted lines. The black dotted line is the simplified expression for short time given by (10).

From (9a), we notice that \overline{h}_s is a function dependent on \overline{l}_c only. This is because that at short times, the gel behaves as an incompressible elastic solid with $v^e = 0.5$, independent of the drained Poisson's ratio v. In a previous work, this feature allowed us to use (9a) to extract the magnitude of surface stress, provided that \overline{h}_s , w and G were known. The short-time surface height \overline{h}_s and wavelength 2w can be measured, for example, by optical interferometry, and the shear modulus G of the gel can be obtained independently in a separate test. To avoid evaluating the series (9a), we provide an approximate expression for the short time surface height, i.e.,

$$\bar{h}_s^{appr} = 0.5997 \bar{l}_c^2 - 1.055 \bar{l}_c + 1. \tag{10}$$

The prediction of (10) is plotted in Fig. 2(b) as a black dotted line. It agrees with the analytical solutions and FEM well. Equation (10) allows one to determine \bar{l}_c from \bar{h}_s .

The drained Poisson's ratio can be determined using \overline{h}_s and \overline{h}_l . To see this, (9b) implies that \overline{h}_l depends on both \overline{l}_c and v. Let us suppose that \overline{l}_c has been determined using \overline{h}_s measured in experiment (using (10)), then one can determine v by substituting \overline{l}_c into (9b). This relation between \overline{h}_s , \overline{h}_l and v is given graphically in Fig. 3. Using this contour map, one can determine the drained Poisson's ratio from measured values of \overline{h}_s and \overline{h}_l . It should be noted that, unlike the procedure of determining the surface stress where a separate test is needed to measure the shear modulus, the drained Poisson's ratio can be completely determined by measuring the surface heights at short and long times in experiments.

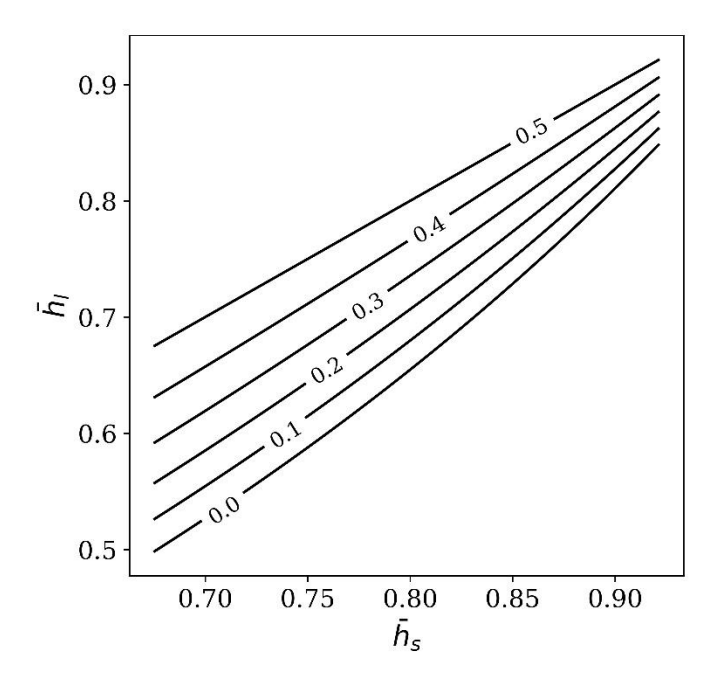


Fig. 3. Contour plots for normalized short- and long-time normalized height of the channel-ridge surface in which each contour line corresponds to a drained Poisson ratio ν of the gel.

4.2 Relative Height Relaxation Curve

In the previous section we have provided a procedure by which the elasto-capillary number (and hence the surface stress) and the drained Poisson's ratio v can be determined using \overline{h}_s and \overline{h}_l measured in experiments. In this section we show that the diffusivity of the gel, D_c , can also be determined by measuring a quantity called relative surface height, which is defined as $\theta = (\overline{h} - \overline{h}_l)/(\overline{h}_s - \overline{h}_l)$. This dimensionless quantity reflects the transient surface flattening process over time; θ relaxes from one to zero as the gel approaches equilibrium.

A straightforward dimensional analysis implies

$$\theta = f\left(\frac{h_0}{w}, \frac{l_c}{w}, \nu, \overline{t}\right),\tag{11}$$

where f is a dimensionless function. Fig. 4(a) shows that θ is insensitive to h_0/w as long as $h_0/w <<1$. To investigate the surface stress effect on θ , represented by elastocapillary number $\overline{l}_c (= l_c/w)$, we plot θ against \overline{t} for different \overline{l}_c in Fig. 4(b). The elastocapillary number \overline{l}_c is chosen to be between 0.1 to 0.4, which are typical values observed in experiments 2,5,32 . The drained Poisson's ratio is 0.2 in these simulations. From Fig. 4(b), it is evident that the effect of \overline{l}_c on the relative surface height versus time is small, in the sense that the maximum difference of \overline{t} (for a fixed value of θ) for different curves is much less than the total time (over 7 decades)

where the variation occurs. Fig. 4(b) also shows that the gel reaches equilibrium when \bar{t} is on the order of one. This confirms that our conjecture that the characteristic time t^* should scale with the wavelength 2w.

The number of arguments in (11) is now narrowed down to two; that is,

$$\theta = f\left(v, \overline{t}\right). \tag{12}$$

We plot the relative surface height relaxation curve for different drained Poisson's ratios ν in Fig. 5(a). It shows that the characteristic time to equilibrate decreases as ν increases, which is to be expected. This is because when $\nu=0.5$, the time it takes to equilibrate is zero as the gel surface height cannot be further reduced by surface stress. More interestingly, we observe that the curves for different ν are parallel – suggesting a master curve can be produced by shifting the curves horizontally in a log-log plot. We find that if a new characteristic time is defined as $t^{**} \equiv (0.5 - \nu) w^2 / D_c$, and we re-normalize time t by

$$\overline{t}^{\text{new}} \equiv \frac{t}{t^{**}} = \frac{D_c t}{(0.5 - v)w^2},$$
(13)

the relative height relaxation curves corresponding to different ν collapse to one single curve, as shown in Fig. 5(b). This rescaling indicates that θ is a function of a single dimensionless time. A fit for the master curve is

$$\theta = f\left(\overline{t}^{\text{new}}\right) = \exp\left(-2.674\overline{t}^{\text{new}} - 1.647\sqrt{\overline{t}^{\text{new}}}\right) \tag{14}$$

which is plotted as symbols in Fig. 5(b). Remarkably, (14) provides a very good fit to the FEM results for all \bar{t}^{new} . The usefulness of this result is that the diffusivity D_c can be obtained by comparing the experimentally measured time dependence of the relative height relaxation curve to (14). Similar to the procedure to extract the drained Poisson's ratio, the cooperative diffusivity D_c of the gel can be determined by the graphing surface height versus time. It is not necessary to measure any other material properties.

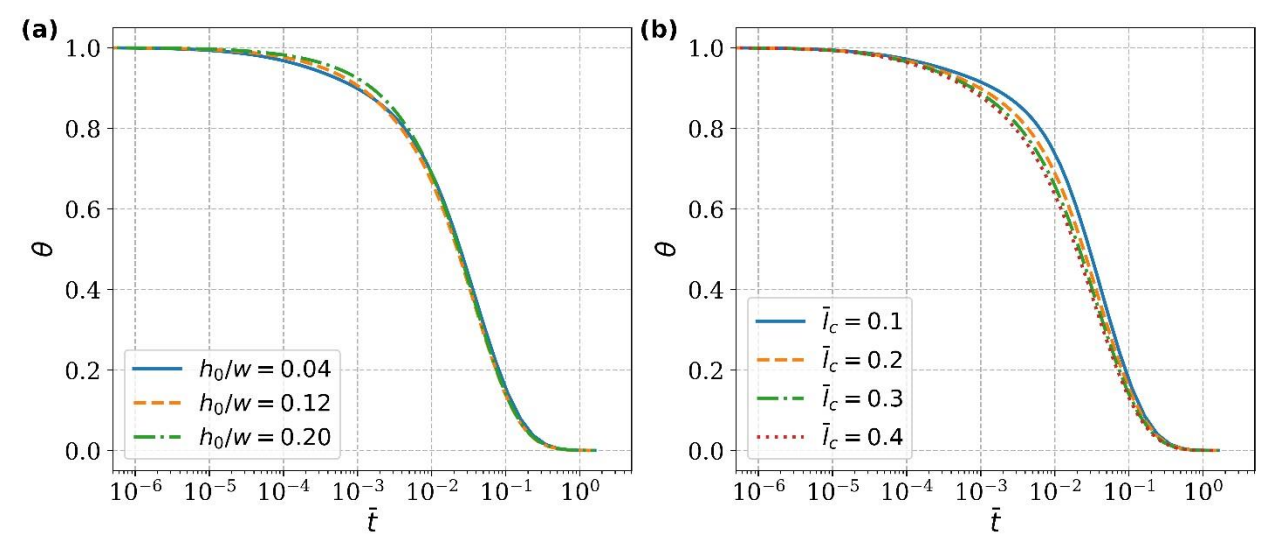


Fig. 4. The relative surface height θ is approximately independent of (a) height and (b) elasto-capillary number.

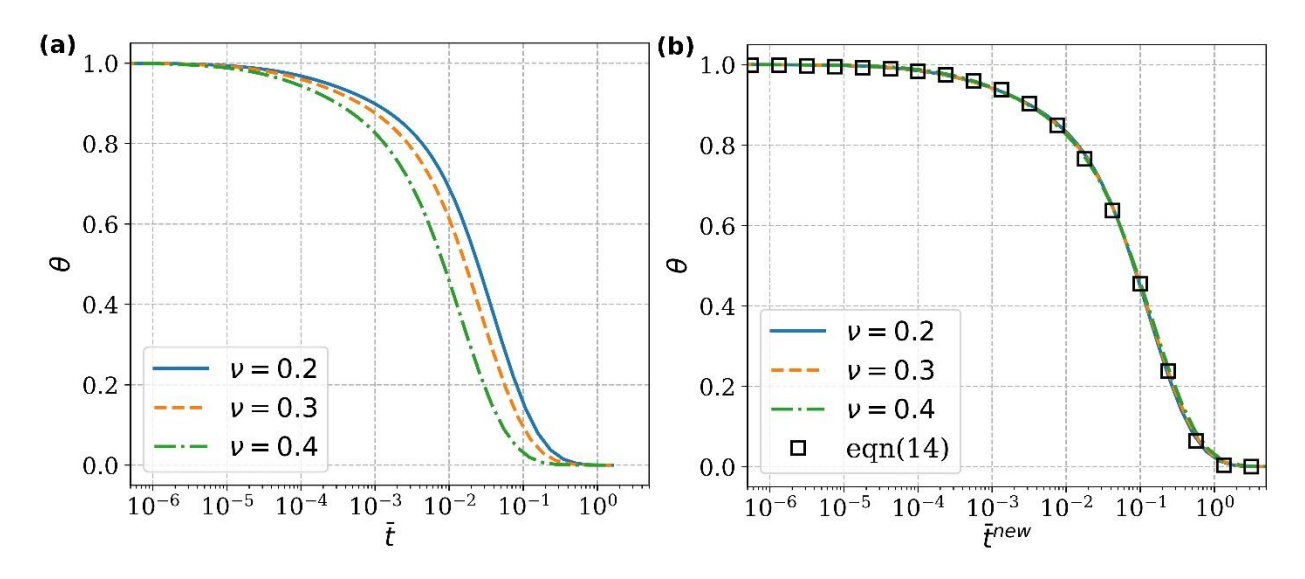


Fig. 5. (a) θ versus normalized time $\overline{t} = t/t^*$. (b) θ plotted against new normalized time $\overline{t}^{new} = t/t^{**}$. The square symbols are obtained from eq. (14).

5. Summary and Discussion

In this work, we have proposed a test by which the surface stress, the drained Poisson's ratio and the diffusivity of a gel can be measured simultaneously. This test is based on measuring the time-dependent surface profile of a periodic ridge-channel gel structure. The time dependence of the surface profile is due to poroelastic flow caused by the flattening effect of surface stress. We carried out finite element analysis to support our analysis. The determination of surface stress requires knowledge of the shear modulus. However, the drained Poisson's ratio and the diffusivity can be obtained with no mechanical testing.

We illustrate more quantitatively how this might work experimentally. For a typical hydrogel, the diffusivity is on the order of $D_c \approx 10^{-11}$ m²/s ^{68–70}. A typical value for surface stress is $\sigma_s \approx 70$ mN/m. If we use a periodic ridge-channel geometry with height $h_0 \approx 0.1$ mm and wavelength 2w of 1 mm, then the elasto-capillary number $\overline{l}_c \equiv \sigma_s / Gw$ for samples of this geometry is on the order of $\frac{140 \text{ Nm}^{-2}}{G}$. For a hydrogel with modulus on the order of kPa, the elasto-capillary number is of order 0.1. The characteristic relaxation time $t^{**} \sim w^2 / D_c \sim 10^4 \text{ s}$. This time scale allows sufficient time to perform the measurements. For example, to capture the full time-dependent behavior of the relative height curve, an image exposure time of 1s is necessary. In modern image technologies (e.g., high speed video microscopy), images can be easily acquired with 1 μ s exposure time t_0^{50} , which is more than sufficient for our needs. To measure smaller structures, one can decrease diffusivity by replacing water with a water-glycerol mixture to swell the gel t_0^{71} . The pure glycerol solvent will increase the viscosity and hence decrease

the diffusivity by three orders of magnitude. This justifies the feasibility of using surface flattening method to determine both poroelastic and surface material properties in experiments.

It is also interesting to note that for sufficiently large elastocapillary number $\overline{l_c} >> 1$, the series of the final equilibrium shape obtained using (8) is given by

$$\overline{s}\left(\overline{y}_{1}, \overline{l}_{c} >> 1\right) \approx \frac{1}{2} + \frac{2}{\pi^{2}(1-\nu)\overline{l}_{c}} \chi(\overline{y}_{1}), \tag{15a}$$

where

$$\chi\left(\overline{y}_{1}\right) = \sum_{n=0}^{\infty} \frac{\left(-1\right)^{n}}{\left(2n+1\right)^{2}} \cos\left(n\pi\overline{y}_{1}\right). \tag{15b}$$

In particular, the normalized peak to valley height is inversely proportional to \overline{l}_c and is given by

$$\overline{h}\left(\overline{l_c} >> 1\right) \approx \frac{4}{\pi^2 (1-\nu) \overline{l_c}} \sum_{n=0}^{\infty} \frac{(-1)^n}{(2n+1)^2} = \frac{4C}{\pi^2 (1-\nu) \overline{l_c}},$$
(15c)

where C = 0.9159655941... is the Catalan's constant.

In this work, we assume that the material is linear poroelastic. However, soft solids can exhibit viscoelastic behaviors. Viscoelastic relaxation decreases the shear modulus, resulting in increasing elastocapillary length with time and promoting the flattening effect of surface stress. In contrast to the poroelastic relaxation time, which is quadratic in the sample wavelength, the viscoelastic relaxation time is independent on the geometry. Thus, one can experimentally distinguish between the surface height relaxation due to solvent flow and surface height relaxation due to viscoelastic relaxation of the gel networks. The coupling of poroelastic and viscoelastic effects at the same time scale is beyond the scope of this work, and it needs to be studied in the future work.

Another limitation in our model is that surface stress is assumed to be isotropic and constant, and large deformation effect is completely ignored in our analysis. In addition, it is known that surfaces of very soft polymers can have significant surface elasticity (the "Shuttleworth Effect" ⁷²), and small strain linear elasticity theory is no longer valid when the ridge-channel structure becomes deep ⁵. One approach is to use numerical methods like nonlinear finite element modeling. A few nonlinear transient finite element methods to study coupled solvent diffusion and large deformation have been developed recently ^{45,73,74}. One can supplement these models with a surface finite-element model to study the complicated surface flattening relaxation process.

Further, we assume that the squeezed-out solvent is sufficient thin (not filling up the valleys) so that the surface stress still exists to drive the deformation. To justify this assumption, we first plot the solvent flux field \mathbf{j} on the interface at time $\overline{t}^{\text{new}} = 10^{-3}$ and $\overline{t}^{\text{new}} = 1$ in Fig. 6. We use $h_0 / w = 0.04$, $\overline{l}_c = \sigma_s / Gw = 0.2$, and

v = 0.2 in the FE simulation, and normalize the solvent flux by $k_w G / \gamma_w w$, i.e., the normalized flux $\mathbf{J} = \frac{\gamma_w w}{k_w G} \mathbf{j}$.

The direction and magnitude of the normalized flux field is indicated by the red arrows in Figure 6. The magnitude of the flux is actually very small, since the flux is normalized by $\frac{k_w G}{\gamma_w w} = \frac{(1-2v)D_c}{2(1-v)w}$. If we take $D_c \approx 10^{-11}$ m²/s

and 2w = 1 mm, a normalized flux value of 1 corresponds to 10^{-8} m/s. At very short times ($\overline{t}^{\text{new}} = 10^{-3}$), the solvent is leaving the gel on the top surface and the maximum outward flux occurs at the top corner, while the solvent is entering the gel on the bottom surface and the maximum inward flux occurs at the bottom corner. At the characteristic time ($\overline{t}^{\text{new}} = 1$), the flux becomes negligible and a different feature emerges: the maximum outward and inward fluxes occur at the peak and valley of the surface, respectively. Integration of the solvent flux over the time and the entire interface gives the total volume change of the solvent. We find that the total volume leaving the gel till a very long time $\overline{t}^{\text{new}} = 5$ is about $0.029h_0w$, which is negligible compared to the sample size. It lends support to our assumption.

Finally, future work needs to consider more realistic boundary conditions which allow for non-equilibrium drying of the gel.

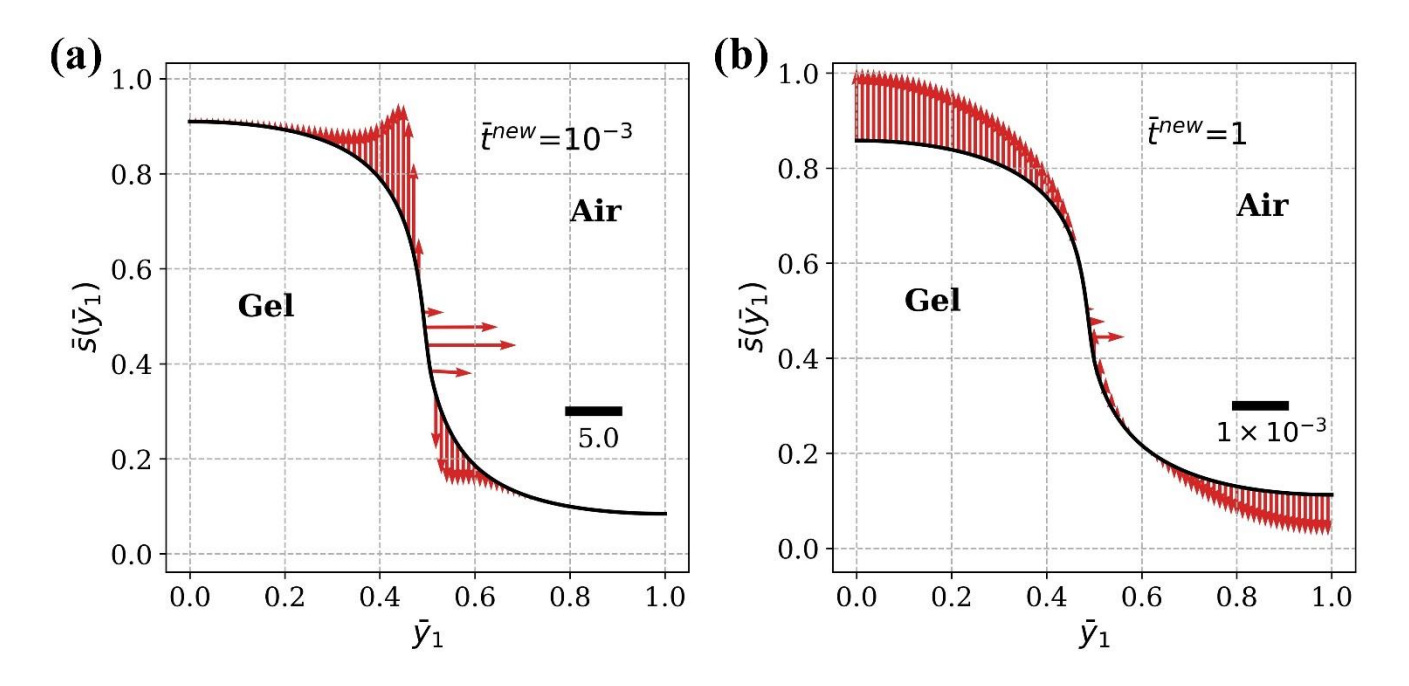


Fig. 6. Normalized flux at time (a) $\overline{t}^{\text{new}} = 10^{-3}$ and (b) $\overline{t}^{\text{new}} = 1$. The black curve is the deformed surface profile of the ridge-channel structure. The red arrows represent the direction and magnitude of the flux and the scale bar in (a) and (b) indicates the magnitude of the flux.

Conflicts of interest:

There are no conflicts of interest to declare.

Acknowledgements:

CYH is supported by National Science Foundation, USA MoMS program under grant number 1903308. JPG thanks the financial support from Japan Society for the Promotion of Science (JSPS) KAKENHI (grant no. JP17H06144).

References

- 1 B. Andreotti and J. H. Snoeijer, Annu. Rev. Fluid Mech., 2020, 52, 285–308.
- 2 R. W. Style, A. Jagota, C.-Y. Hui and E. R. Dufresne, *Annual Review of Condensed Matter Physics*, 2017, **8**, 99–118.
- 3 A. Marchand, S. Das, J. H. Snoeijer and B. Andreotti, *Phys. Rev. Lett.*, 2012, **108**, 094301.
- 4 S. Mora, C. Maurini, T. Phou, J.-M. Fromental, B. Audoly and Y. Pomeau, *Phys. Rev. Lett.*, 2013, **111**, 114301.
- 5 D. Paretkar, X. Xu, C.-Y. Hui and A. Jagota, Soft Matter, 2014, 10, 4084–4090.
- 6 S. Mora, T. Phou, J.-M. Fromental, L. M. Pismen and Y. Pomeau, *Phys. Rev. Lett.*, 2010, **105**, 214301.
- 7 R. W. Style, R. Boltyanskiy, B. Allen, K. E. Jensen, H. P. Foote, J. S. Wettlaufer and E. R. Dufresne, *Nature Physics*, 2014, **11**, 82–87.
- 8 C.-Y. Hui, T. Liu and M.-E. Schwaab, Extreme Mechanics Letters, 2016, 6, 31–36.
- 9 C. I. Kim, P. Schiavone and C.-Q. Ru, *Journal of Elasticity*, 2011, **104**, 397–420.
- 10R. Thomson, T.-J. Chuang and I.-H. Lin, *Acta Metallurgica*, 1986, **34**, 1133–1143.
- 11 Z. Cao, M. J. Stevens and A. V. Dobrynin, *Macromolecules*, 2014, 47, 3203–3209.
- 12J.-M. Y. Carrillo and A. V. Dobrynin, *Langmuir*, 2012, **28**, 10881–10890.
- 13 Z. Liu, K. E. Jensen, Q. Xu, R. W. Style, E. R. Dufresne, A. Jagota and C.-Y. Hui, *Soft Matter*, 2019, **15**, 2223–2231.
- 14T. Salez, M. Benzaguen and É. Raphaël, Soft Matter, 2013, 9, 10699.
- 15 R. W. Style, C. Hyland, R. Boltyanskiy, J. S. Wettlaufer and E. R. Dufresne, *Nature Communications*, 2013, 4, 2728.
- 16 X. Xu, A. Jagota and C.-Y. Hui, Soft Matter, 2014, 10, 4625–4632.
- 17I. Ang, Z. Liu, J. Kim, C.-Y. Hui and N. Bouklas, *Journal of the Mechanics and Physics of Solids*, 2020, **145**, 104132.
- 18Z. Liu, N. Bouklas and C.-Y. Hui, *Proceedings of the Royal Society A: Mathematical, Physical and Engineering Sciences*, 2020, **476**, 20190761.
- 19Z. Cao and A. V. Dobrynin, *Macromolecules*, 2015, **48**, 443–451.
- 20 J. Dervaux and L. Limat, *Proceedings of the Royal Society A: Mathematical, Physical and Engineering Sciences*, 2015, **471**, 20140813.
- 21 E. R. Jerison, Y. Xu, L. A. Wilen and E. R. Dufresne, *Phys. Rev. Lett.*, 2011, **106**, 186103.
- 22L. Limat, The European Physical Journal E, 2012, 35, 134.
- 23 T. Liu, Z. Liu, A. Jagota and C.-Y. Hui, Journal of the Mechanics and Physics of Solids, 2020, 138, 103902.
- 24 A. Marchand, S. Das, J. H. Snoeijer and B. Andreotti, *Physical Review Letters*, 2012, **109**, 236101.
- 25 J. Olives, J. Phys.: Condens. Matter, 2010, 22, 085005.

- 26J. H. Snoeijer, E. Rolley and B. Andreotti, *Phys. Rev. Lett.*, 2018, **121**, 068003.
- 27R. W. Style, R. Boltyanskiy, Y. Che, J. S. Wettlaufer, L. A. Wilen and E. R. Dufresne, *Phys. Rev. Lett.*, 2013, 110, 066103.
- 28 H. Wu, Z. Liu, A. Jagota and C.-Y. Hui, Soft Matter, 2018, 14, 1847–1855.
- 29 K. E. Jensen, R. W. Style, Q. Xu and E. R. Dufresne, *Physical Review X*, 2017, 7, 041031.
- 30C. M. Stafford, C. Harrison, K. L. Beers, A. Karim, E. J. Amis, M. R. VanLandingham, H.-C. Kim, W. Volksen, R. D. Miller and E. E. Simonyi, *Nature Materials*, 2004, **3**, 545–550.
- 31P.-C. Lin, S. Vajpayee, A. Jagota, C.-Y. Hui and S. Yang, *Soft Matter*, 2008, 4, 1830–1835.
- 32N. Lapinski, Z. Liu, S. Yang, C.-Y. Hui and A. Jagota, *Soft Matter*, 2019, **15**, 3817–3827.
- 33 D. J. Steigmann and R. W. Ogden, *Proceedings of the Royal Society of London. Series A: Mathematical, Physical and Engineering Sciences*, 1999, **455**, 437.
- 34X. Gao, Z. Huang, J. Qu and D. Fang, Journal of the Mechanics and Physics of Solids, 2014, 66, 59–77.
- 35 M. E. Gurtin and A. I. Murdoch, Archive for Rational Mechanics and Analysis, 1975, 57, 291–323.
- 36 A. E. Green, P. M. Naghdi and W. L. Wainwright, *Archive for Rational Mechanics and Analysis*, 1965, **20**, 287–308.
- 37Z. Liu, A. Jagota and C.-Y. Hui, *Soft Matter*, 2020, **16**, 6875–6889.
- 38D. W. Bousfield, Journal of Non-Newtonian Fluid Mechanics, 1991, 40, 47-54.
- 39 C.-Y. Hui and A. Jagota, Journal of Polymer Science Part B: Polymer Physics, 2016, 54, 274–280.
- 40 S. Karpitschka, S. Das, M. van Gorcum, H. Perrin, B. Andreotti and J. H. Snoeijer, *Nature Communications*, 2015, **6**, 7891.
- 41 R. Keunings and D. W. Bousfield, Journal of Non-Newtonian Fluid Mechanics, 1987, 22, 219–233.
- 42 W. W. Mullins, Journal of Applied Physics, 1959, 30, 77–83.
- 43 S. E. Orchard, Applied Scientific Research, Section A, 1963, 11, 451–464.
- 44Q. Xu, L. A. Wilen, K. E. Jensen, R. W. Style and E. R. Dufresne, *Phys. Rev. Lett.*, 2020, **125**, 238002.
- 45 N. Bouklas, C. M. Landis and R. Huang, Journal of the Mechanics and Physics of Solids, 2015, 79, 21–43.
- 46 N. Bouklas and R. Huang, Soft Matter, 2012, 8, 8194.
- 47 W. Hong, X. Zhao, J. Zhou and Z. Suo, *Journal of the Mechanics and Physics of Solids*, 2008, **56**, 1779–1793.
- 48 Y. Hu, X. Zhao, J. J. Vlassak and Z. Suo, Appl. Phys. Lett., 2010, 96, 121904.
- 49C.-Y. Hui, Y. Y. Lin, F.-C. Chuang, K. R. Shull and W.-C. Lin, *Journal of Polymer Science Part B: Polymer Physics*, 2006, 44, 359–370.
- 50 J. D. Berman, M. Randeria, R. W. Style, Q. Xu, J. R. Nichols, A. J. Duncan, M. Loewenberg, E. R. Dufresne and K. E. Jensen, *Soft Matter*, 2019, **15**, 1327–1334.
- 51 M. Zhao, F. Lequeux, T. Narita, M. Roché, L. Limat and J. Dervaux, Soft Matter, 2018, 14, 61–72.
- 52 G. A. Busby, M. H. Grant, S. P. MacKay and P. E. Riches, Journal of Biomechanics, 2013, 46, 837–840.
- 53 Q. T. Nguyen, Y. Hwang, A. C. Chen, S. Varghese and R. L. Sah, *Biomaterials*, 2012, 33, 6682–6690.
- 54G. W. Scherer, Journal of Non-Crystalline Solids, 1992, 142, 18–35.
- 55 D. A. Berk, F. Yuan, M. Leunig and R. K. Jain, *Biophysical journal*, 1993, **65**, 2428–2436.
- 56 J. P. Gong, N. Hirota, A. Kakugo, T. Narita and Y. Osada, J. Phys. Chem. B, 2000, 104, 9904–9908.
- 57 S. J. Gibbs, E. N. Lightfoot and T. W. Root, *The Journal of Physical Chemistry*, 1992, **96**, 7458–7462.
- 58 A. Jagota, D. Paretkar and A. Ghatak, Phys. Rev. E, 2012, 85, 051602.
- 59M. A. Biot, Journal of Applied Physics, 1955, 26, 182–185.
- 60 M. A. Biot, Journal of Applied Physics, 1941, 12, 155–164.
- 61 J. McNamee and R. E. Gibson, *The Quarterly Journal of Mechanics and Applied Mathematics*, 1960, **13**, 98–111.
- 62 J. R. Rice and M. P. Cleary, *Reviews of Geophysics*, 1976, 14, 227–241.
- 63 X. Gao and W. Gu, Journal of Biomechanics, 2014, 47, 3196–3200.
- 64R. M. Hodge, T. J. Bastow, G. H. Edward, G. P. Simon and A. J. Hill, *Macromolecules*, 1996, **29**, 8137–8143.
- 65 R. Meacham, M. Liu, J. Guo, A. T. Zehnder and C.-Y. Hui, Exp Mech, 2020, 60, 1161–1165.

- 66M. Y. Truong, N. K. Dutta, N. R. Choudhury, M. Kim, C. M. Elvin, K. M. Nairn and A. J. Hill, *Biomaterials*, 2011, **32**, 8462–8473.
- 67 C.-Y. Hui, Z. Liu, N. Bain, A. Jagota, E. R. Dufresne, R. W. Style, R. Kiyama and J. P. Gong, *Proc. R. Soc. A.*, 2020, **476**, 20200477.
- 68E. Axpe, D. Chan, G. S. Offeddu, Y. Chang, D. Merida, H. L. Hernandez and E. A. Appel, *Macromolecules*, 2019, **52**, 6889–6897.
- 69 K. B. Kosto and W. M. Deen, AIChE Journal, 2004, 50, 2648–2658.
- 70 S. Mora, E. Andò, J.-M. Fromental, T. Phou and Y. Pomeau, Soft Matter, 2019, 15, 5464–5473.
- 71 P. N. Shankar and M. Kumar, *Proceedings of the Royal Society of London. Series A: Mathematical and Physical Sciences*, 1994, **444**, 573–581.
- 72 R. Shuttleworth, *Proceedings of the Physical Society. Section A*, 1950, **63**, 444.
- 73 S. A. Chester, C. V. Di Leo and L. Anand, *International Journal of Solids and Structures*, 2015, **52**, 1–18.
- 74J. Zhang, X. Zhao, Z. Suo and H. Jiang, Journal of Applied Physics, 2009, 105, 093522.